AIAA JOURNAL
Vol. 38, No. 3, March 2000

Large Eddy Simulation in Complex Geometric Configurations Using Boundary Body Forces

Roberto Verzicco*
Politecnico di Bari, 70125 Bari, Italy
Jamaludin Mohd-Yusof†
Stanford University, Stanford, California 94305
Paolo Orlandi‡
University of Rome "La Sapienza," 00184 Rome, Italy
and
Daniel Haworth§
General Motors Research and Development Center, Warren, Michigan 48090-9055

A numerical method is presented that allows large eddy simulation (LES) of turbulent flows in complex geometric configurations with moving boundaries and that retains the advantages of solving the Navier–Stokes equations on fixed orthogonal grids. The boundary conditions are applied independently of the grid by assigning body forces over surfaces that need not coincide with coordinate lines. The use of orthogonal, nondeforming grids simplifies grid generation, facilitates the implementation of high-order, nondissipative discretization schemes, and minimizes the spatial and temporal variations in filter width that complicate unstructured deforming-grid LES. Dynamic subgrid-scale turbulence models are particularly appealing in combination with the body-force procedure because the dynamic model accounts automatically for the presence of solid walls without requiring damping functions. The method is validated by simulations of the turbulent flow in a motored axisymmetric piston–cylinder assembly for which detailed experimental measurements are available. Computed mean and rms velocity profiles show very good agreement with measured ensemble averages. The present numerical code runs on small, personal computer-like workstations. For a comparable level of accuracy, computational requirements (memory and CPU time) are at least a factor of 10 lower compared to published simulations for the same configuration obtained using an unstructured, boundary-fitted deforming-grid approach.

Introduction

COMPUTATIONAL fluid dynamics (CFD) is increasingly relied on by industry as a key tool in the design and test of products and processes. Computer simulation allows the rapid investigation of wide parameter ranges and the testing of novel technological solutions without resorting to expensive hardware prototypes and measurements. Most flows of practical engineering interest present complications including complex three-dimensional geometric configurations, moving boundaries, and high Reynolds numbers (turbulence).

The most comprehensive, three-dimensional, time-dependent numerical turbulent flow simulations have been limited to simple geometric configurations. In this case, the flow can be represented using a regular orthogonal mesh or basis functions, and high-fidelity spatial and temporal discretizations can be maintained with a small number of operations per node and with low storage requirements. For example, homogeneous isotropic turbulence in a triperiodic box has been simulated using 512^3 nodes or more,[1] and comparably high resolution has been achieved for other simple canonical configurations including planar channel flow and mixing layers.[2,3] In the majority of industrial applications, however, even the simplest flow features cannot be captured if the shape of the domain boundary is not accounted for in detail. As a result, curvilinear boundary-fitted coordinates and unstructured grids are currently the methods of choice for engineering CFD,[4] in spite of their complexity in grid generation, high computational overhead (large number of operations per node and high storage requirements), and generally low-order numerics (second-order dissipative spatial discretizations, with first- or second-order time integration). Given the finite amount of memory and clock cycles available on any computer, the maximum number of nodes that can be used to represent engineering flows is limited. Three-dimensional, time-dependent CFD for practical engineering configurations rarely exceeds 10^6 (100^3) nodes.

Moving and/or deforming flow domains further complicate numerical flow simulation. Nonstationary boundaries are important in an increasing number of CFD applications including positive-displacement pumps, turbomachinery, and reciprocating piston engines. When boundary-fitted meshes are employed, the grid either must be regenerated or deformed as the geometry changes, adding considerably to the computational complexity.

A third point to be considered is the Reynolds number. In most engineering applications, the Reynolds number is far too high to resolve all relevant spatial and temporal scales directly without turbulence modeling [direct numerical simulations (DNS)]. Instead, the range of scales to be resolved is reduced by filtering the governing equations and modeling the resulting additional terms that arise; these terms represent apparent stresses from velocity fluctuations about the filtered mean. In Reynolds-averaged Navier–Stokes (RANS) modeling, all fluctuations about the ensemble-averaged mean are dealt with by the turbulence model; in large eddy simulation (LES), fluctuations at scales smaller than a prescribed filter width are modeled using subfilter-scale (subgrid-scale) models.[5] In a growing number of engineering applications, turbulence modeling is evolving from RANS towards LES.[6,7] An important distinction between RANS and LES is the sense in which a numerical solution converges with decreasing mesh size and computational time step.

Received 4 February 1999; revision received 20 June 1999; accepted for publication 22 June 1999.

*Associate Professor, Istituto di Macchine ed Energetica, Via Re David 200.

†Postdoctoral Research Fellow, Center for Turbulence Research; currently Postdoctoral Research Fellow, Los Alamos National Laboratory, P.O. Box 1663 IGPP, MS C305, Los Alamos, NM 87545.

‡Full Professor, Dipartimento di Meccanica e Aeronautica, Via Eudossiana 18.

§Researcher, Engine Research Department, Mail Code 480-106-252, 30500 Mound Road 106, Box 9055.

A consistent RANS method converges to an exact solution of the filtered Navier–Stokes equations, whereas a consistent LES method converges to an exact solution of the unfiltered equations, that is, to DNS.

From these observations, it is clear that the availability of high-accuracy, high-efficiency alternatives to current unstructured boundary-fitted deforming-grid methods would represent a significant advance in engineering CFD. Methods that retain the computational efficiency and accuracy of structured orthogonal grids appear to be particularly compelling. Also, compatible subgrid-scale turbulence models for the LES of complex industrial flows are required at the same time.

In this paper we introduce an LES procedure that retains the advantages of fixed orthogonal grids while allowing the simulation of arbitrary geometric configurations with moving boundaries. Specifically, we formulate and demonstrate a method in which boundary conditions are assigned independently of the grid by prescribing suitable body forces. These forces are prescribed in a manner that yields a desired velocity value on a given surface; the surface need not coincide with the coordinate lines and is free to move in time.

The idea of using body forces on a Cartesian mesh to mimic complex geometric boundaries is not, in itself, new. Peskin[8] introduced a similar approach. And more recently Goldstein et al.[9] and Saiki and Biringen[10] have published further examples. The main drawback in all cases has been a significant reduction in the stability limit of the time-integration scheme with forcing. Goldstein et al.,[9] for example, point out that their computational time step was limited to a material Courant–Friedrichs–Lewy (CFL) number[11] of 0.004–0.04 in computations of flow about a right circular cylinder. This effectively limits the technique to two-dimensional computations.

A different expression for the forcing was suggested by Mohd-Yusof[12,13] and Mohd-Yusof and Lumley.[14,15] In computations of laminar flow over a riblet and the flow around circular cylinders, they demonstrated that the stability limit of their integration scheme was essentially unaffected by the forcing. The Mohd-Yusof (MY) forcing was implemented by Fadlun et al.[16,17] There it was demonstrated that results remained essentially the same as those obtained using an alternative method and that the time step remained large enough to make three-dimensional simulations practical. As will be seen later, this is possible because the latter forcing does not introduce additional terms in the equations, but it only enforces a velocity value over the immersed boundary by deleting preexisting terms of the equations.

Although the MY forcing method is in principle very general, to our knowledge it has never before been applied to a complex three-dimensional flow configuration with moving boundaries at a Reynolds number sufficiently high to require a turbulence model and where comprehensive experimental measurements are available for quantitative validation. Here computations are reported for a motored piston–cylinder assembly [an idealized reciprocating integrated circuit (IC) engine] at a Reynolds number sufficiently high to require a turbulence model: A subgrid-scale LES turbulence modeling approach is adopted. Computed results are compared with experimental measurements obtained by Morse et al.[18] The present results also are compared with previously published LES for the same configuration that used an unstructured boundary-fitted deforming-grid approach.[7,19]

Flow Configuration

The geometric configuration is an axisymmetric piston–cylinder assembly with flat cylinder head and piston and a fixed central valve (Fig. 1). In the experiment[16] the piston is externally driven in simple harmonic motion at a speed of 200 rpm ($\simeq$21 rad/s), yielding a mean piston speed of $\bar{V}_p = 0.4$ m/s. There is no compression; air flows into the cylinder during the downward stroke of the piston and out of the cylinder during the piston upstroke. The Reynolds number based on bore diameter and mean piston speed is $Re = \bar{V}_p b/\nu = \Omega s r_r/(15\nu) \approx 2000$ (Ω in rpm, $\nu = 1.5 \times 10^{-5}$ m^2/s).

Morse et al.[18] used laser-Doppler anemometry to measure ensemble- (phase-) averaged mean and rms radial profiles of the axial velocity component. Profiles are available at 10-mm axial increments starting from the cylinder head for crank positions of 36, 90, 144, and 270 deg after piston top dead center (TDC). This configuration has been the subject of exhaustive modeling studies using both RANS- and LES-based turbulence models.[7,19,20]

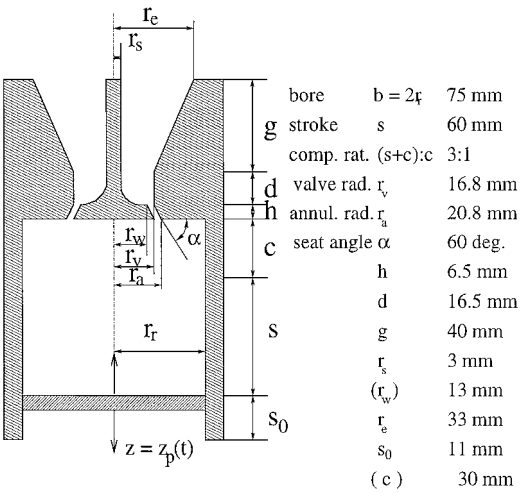

Fig. 1 Axisymmetric piston–cylinder assembly of Morse et al.[17]

Governing Equations and Numerical Methodology

The relevant equations for LES are the filtered Navier–Stokes equations. An additional boundary body-force term $\boldsymbol{f}$ is added to the incompressible form to yield

$$\frac{\mathrm{D}\bar{\boldsymbol{u}}}{\mathrm{D}t} = -\rho^{-1}\nabla\bar{P} + \nabla\cdot\{\tilde{\nu}[\nabla\bar{\boldsymbol{u}} + (\nabla\bar{\boldsymbol{u}})^T]\} + \boldsymbol{f} \tag{1a}$$

$$\nabla\cdot\bar{\boldsymbol{u}} = 0 \tag{1b}$$

Here $\bar{\boldsymbol{u}}$ denotes the filtered velocity, and $\bar{P}$ is the sum of the filtered pressure and the trace of the subgrid-scale stress tensor. The anisotropic part of the subgrid-scale stress q_{ij} is modeled using a Smagorinsky subgrid-scale model $q_{ij} = -2\nu_t\bar{S}_{ij}$, where the subgrid-scale turbulent viscosity is $\nu_t = C\Delta^2(2\bar{S}_{ij}\bar{S}_{ij})^{1/2}$, $\bar{S}_{ij}$ is the filtered rate-of-strain tensor, and Δ is the filter width being defined as twice the computational cell in all directions. The effective viscosity $\tilde{\nu}$ is the sum of the subgrid-scale viscosity ν_t and the fluid viscosity: $\tilde{\nu} = \nu_t + \nu$.

The value of the model coefficient C in the subgrid-scale turbulent viscosity ν_t is determined by a dynamic procedure[21,22] that does not require the direct specification of any model constants. Essentially, this involves filtering at two different length scales or filter widths. The first filtering operation is implicit in the numerical method and corresponds to a filter width that is equal to the local grid spacing. The second filter (the test filter) is implemented by averaging over nearest-neighbor nodes; this corresponds to a filter width of twice the local grid spacing. Finally, an average over statistically homogeneous directions is needed to determine the local value of C. For the present axisymmetric configuration, this final averaging is done in the azimuthal direction. All points having a total effective viscosity $\tilde{\nu}$ that is smaller than zero are clipped to zero viscosity; the percentage of clipped nodes never exceeds 3% for the computations reported here. Provided that grid resolution is adequate in the vicinity of solid walls, this form of the dynamic model properly accounts for wall proximity without explicit damping functions, for example, the van Driest function in the case of a Smagorinsky model.[23] This implies that few gridpoints (typically five or six) should be clustered near the immersed boundary, and this is not always simple owing to the rectangular mesh and the curvilinear boundary.

The boundary body force $\boldsymbol{f}$ is prescribed at each time step to establish the desired velocity $\bar{\boldsymbol{v}}_b$ on an arbitrary surface that need not coincide with coordinate lines. Following Mohd-Yusof,[12] the time-discretized version of Eq. (1a) can be written as

$$\bar{\boldsymbol{u}}^{n+1} - \bar{\boldsymbol{u}}^n = \Delta t(\mathrm{RHS} + \boldsymbol{f}) \tag{2}$$

where Δt is the computational time step; the right-hand side (RHS) contains the nonlinear, pressure, and viscous terms; and the superscript denotes the time-step level. To impose $\bar{\boldsymbol{u}}^{n+1} = \bar{\boldsymbol{v}}_b$, the body force $\boldsymbol{f}$ must be

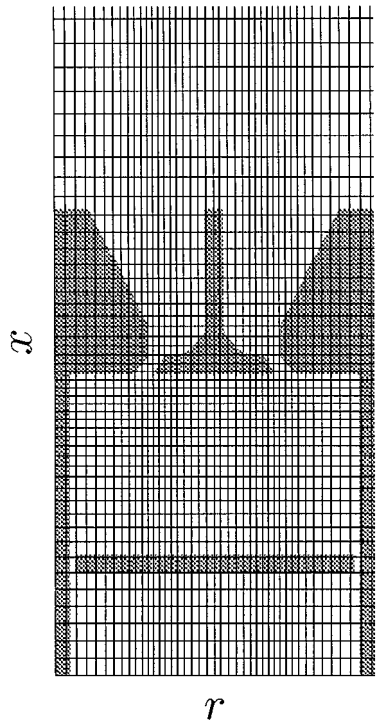

Fig. 2 Vertical section through meridional planes of the computational grid $\theta = 0$ and π; the body-force distribution used to mimic the geometric configuration of Fig. 1 is indicated by the shaded regions, and only one of every four grid points is shown for clarity.

$$f = -\text{RHS} + \frac{\bar{v}_b - \bar{u}^n}{\Delta t} \tag{3}$$

in the flow region where we wish to mimic the solid body and zero elsewhere. In general, the surface of the region where $\bar{u}^{n+1} = \bar{v}_b$ does not coincide with a coordinate line (Fig. 2). In that case, the value of f at the node closest to the surface, but inside the solid body is linearly interpolated between the value that yields $\bar{v}_b$ inside the solid body and the zero value in the interior of the flow domain. This interpolation procedure is consistent with a centered second-order, finite difference approximation, and the overall accuracy of the scheme remains second order.[16,17] It should be stressed that, with the forcing of Eq. (3), steady and moving boundaries are treated in the same way, being in the first case $\bar{v}_b = 0$ and in the latter $\bar{v}_b \neq 0$. For the moving boundary, however, at each time step the set of grid points over which f is applied must be recomputed because a different region of space is affected by the presence of the body. Another important point is that, although for the forcings described in Refs. 9 and 10 the velocity at the immersed boundaries was imposed by additional forces, in this case the velocity is simply driven to the desired value by canceling a few terms in the equations. This implies that, in contrast to the former methods, in the latter case the stability limit of the integration scheme is the same as that without immersed boundaries, thus making practical the simulation of complex three-dimensional flows. Further details of the immersed boundary technique, together with examples with boundaries never aligned with the computational grid, are given in Refs. 16 and 17.

Equations (1) have been spatially discretized in a polar cylindrical coordinate system using staggered, central, second-order, finite difference approximations. Details of the numerical method are given by Verzicco and Orlandi[24]; only the main features are summarized here. In a three-dimensional inviscid flow, kinetic energy is conserved, and this feature is retained in the discretized equations. This is possible because, although the radial momentum equation is written for the quantity $q_r = ru_r$ (Ref. 24), the discretization of the nonlinear terms is performed considering the quantity u_r. For the present code this was proved numerically by Orlandi and Fatica,[25] who showed the conservation of the kinetic energy for a turbulent pipe flow in the limit of an infinite Reynolds number. It has been argued that nondissipative numerical schemes are advantageous compared to upwind-biased schemes for LES.[26] The discretized system is integrated in time using a fractional-step method where the viscous terms are computed implicitly and the convective terms explicitly. The large sparse matrix resulting from the implicit terms is inverted by an approximate factorization technique. At each time step the momentum equations are provisionally advanced using the pressure at the previous time step, giving an intermediate nonsolenoidal velocity field. A scalar quantity Φ is then introduced to project the nonsolenoidal field onto a solenoidal one. The large-band matrix associated with the elliptic equation for Φ is reduced to a pentatridiagonal matrix using trigonometric expansions (fast Fourier transforms) in the azimuthal direction; this matrix is inverted using the FISHPACK package.[27] A hybrid, low-storage, third-order, Runge–Kutta scheme is used to advance the equations in time, and the body forces are enforced at each stage of the Runge–Kutta scheme. Note that the application of f does not require the computation of extra terms but rather the cancellation of preexisting ones. The integration of the equations with the body forces only takes 5% more CPU time than does the integration in the absence of the forcing.

A final consideration is the singularity at $r = 0$. An advantage of the staggered-mesh treatment is that only the radial component of the momentum equation needs to be dealt with at the pole; for this component we calculate the evolution of $q_r = ru_r$ instead of u_r because the former quantity vanishes at $r = 0$.

A cross section through the computational mesh for the configuration of Fig. 1 is shown in Fig. 2. The lower boundary of the computational domain is inflow or outflow, depending on the instantaneous direction of the piston motion, with a prescribed velocity profile. The upper boundary is also an inflow/outflow boundary, but here a convective boundary condition for the velocities is used. The equation solved at the upper boundary for the ith component of velocity u_i is

$$\frac{\partial u_i}{\partial t} + C_i \frac{\partial u_i}{\partial x} = 0 \tag{4}$$

(no summation on i), where C_i is determined explicitly from the previous time step; the computation of the spatial velocity derivative is always the same, regardless of the sign of C_i. The lateral wall of the computational domain is free slip, and all of the no-slip boundary conditions at the surfaces corresponding to solid walls are enforced through the body force f. None of the solid boundaries are coincident with computational nodes.

The laminar axisymmetric cases are started from the fluid at rest, and the initial transient (typically two cycles) is discarded. To save computational time, three-dimensional cases are restarted from a converged, laminar, axisymmetric solution replicated in the azimuthal direction. A random azimuthal velocity perturbation ($|u_\theta|_{\max} = 0.25\bar{V}_p$) is then superposed to initiate three dimensionalities. This procedure reduces the initial transient for the three-dimensional cases to a single cycle.

Results

The flow in a piston engine is fully three dimensional, unsteady, and turbulent; the numerical simulation must cope with all of these aspects. To assess the numerical and modeling procedures outlined in the preceding section, however, we proceed systematically through a hierarchy of cases. A laminar axisymmetric case at a reduced Reynolds number is considered first. This is followed by three-dimensional, reduced-Reynolds-number cases without and with an initial azimuthal velocity perturbation. Finally, the three-dimensional turbulent flow at the Reynolds number of the experiment is simulated.

Low-Reynolds-Number Axisymmetric Simulation

In addition to methodology validation, this case provides insight into the large-scale flow dynamics in the piston–cylinder assembly. These become less clear in the fully turbulent case. The simulation has been run on a grid, 129×385 points in the radial and axial directions, respectively, at a Reynolds number $Re = 625$.

Results are given in the form of azimuthal vorticity maps at six instants over one cycle (Fig. 3). At $t = 0$ (0-deg-piston TDC) the piston starts its downstroke. Fluid is drawn into the cylinder through the annular gap between the fixed central valve and the valve seat in the cylinder head. This generates a high-speed jet that impinges on the cylinder wall and eventually separates as a result of viscous effects. The maximum axial velocity magnitude is approximately

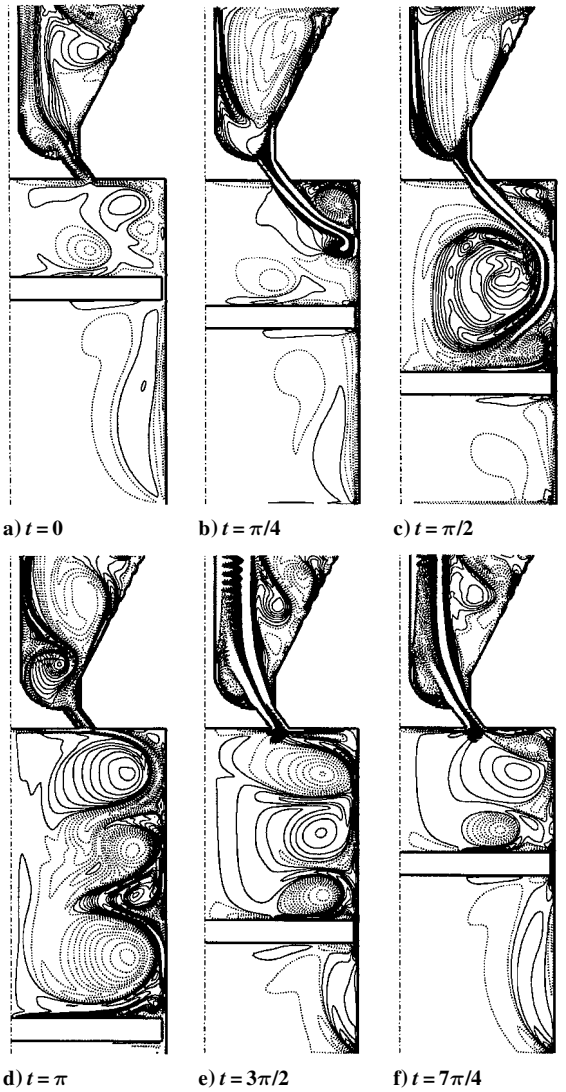

Fig. 3 Contour plots of azimuthal vorticity for a two-dimensional (axisymmetric) laminar case at $Re = 625$, 129×385 grid: ——, positive values; · · · , negative values; and the increment between adjacent isocontours is $\Delta\omega = \pm 2.5\bar{V}_p/b$.

$r_r^2|\ (r_a^2 - r_v^2) = 9.4$ times the instantaneous piston speed; actually, it is somewhat higher as a result of boundary layers that develop on the walls of the annular gap.

At $t = \pi/2$ (90 deg) the jet velocity reaches its maximum, and the in-cylinder flow is dominated by a single toroidal vortex that grows in size as the piston descends. The interaction of the annular jet with the solid walls generates a variety of smaller structures that are already apparent at $t = \pi/2$. Later, as the piston decelerates, the jet does not have enough momentum to penetrate to the piston, and several annular structures are generated close to the valve. The complex flow structure emerging from the interaction of the several recirculating vortices is shown at $t = \pi$ (180 deg) when the piston is at bottom dead center (BDC). As the piston starts its upstroke, these flow structures are pushed out of the cylinder through the annular channel, generating a high-speed jet in the exhaust region. At $t = 7\pi/4$ (315 deg) the piston is nearing its TDC position, and only minor residual motion is left inside the cylinder. A new cycle with similar features begins at $t = 2\pi$ (360 deg).

In addition to the primary in-cylinder flow, there is a secondary flow between the piston and the lower inflow/outflow boundary (Fig. 3). These two flows do not interact because the piston moves as a solid body: There is zero vorticity inside the region corresponding to the piston.

Qualitatively similar in-cylinder flow dynamics were observed for a different axisymmetric motored piston–cylinder assembly by Eaton and Reynolds[28,29] using smoke visualization and high-speed photography. In that experiment, the flow was observed to be complex and three dimensional by piston BDC. Haworth and Jansen's[18] simulations of the Morse et al.[16] configuration showed that flow to be fully three dimensional, and turbulent as well, at the Reynolds number of the experiment. Before proceeding to the fully turbulent case, two intermediate three-dimensional simulations are considered.

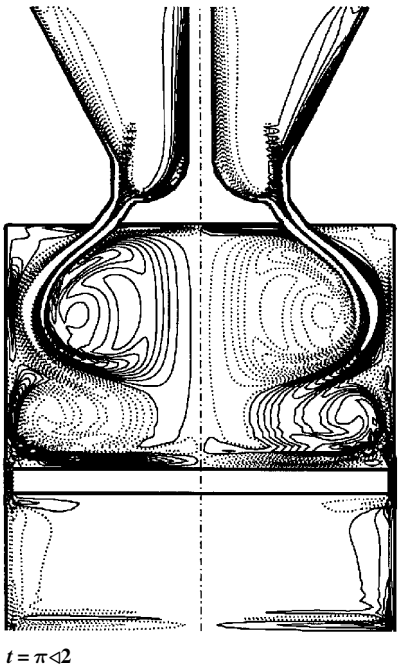

Fig. 4 Contour plots of azimuthal vorticity for a three-dimensional case without azimuthal perturbation at $Re = 315$, $97 \times 85 \times 193$ ($\theta \times r \times z$) grid, $t = \pi/2$, no turbulence model; the vorticity scale is the same as in Fig. 3.

Low-Reynolds-Number, Three-Dimensional Simulations

A three-dimensional simulation without initial azimuthal perturbation was performed at a Reynolds number of $Re = 315$. In this case, the flow remains axisymmetric through at least two full cycles. Figure 4 shows an example of a cross section through the cylinder axis, confirming that flow symmetry is preserved about the geometric axis of symmetry. Here the Reynolds number has been halved with respect to the axisymmetric case of the preceding section. This was necessary to fully resolve all flow scales without resorting to a turbulence model on the $97 \times 85 \times 193$ (aximuthal $\times$ radial $\times$ axial) grid. This case serves to verify that the boundary body forcing does not introduce artificial three dimensionality into the flow.

It might be argued that the reduced Reynolds number is the reason for the observed symmetry conservation. However, a repeat of this simulation with an initial azimuthal perturbation shows that this is not the case (Fig. 5). The instantaneous vorticity snapshots taken from two consecutive cycles demonstrate that strong three dimensionality develops rapidly from the initial perturbation. Moreover, in contrast to the axisymmetric case, the flow does not repeat itself from one cycle to the next. This implies that ensemble, or phase, averages are needed to compute mean quantities and higher-order moments, requiring the simulation of the flow over many cycles. Simulation of higher Reynolds numbers using comparable grid spacings would require a turbulence model.

High-Reynolds-Number, Three-Dimensional LES

For the final simulation, the Reynolds number is increased to the experimental value[16,17] of $Re = 2000$. Two computational meshes of $97 \times 85 \times 193$ and $65 \times 65 \times 151$ nodes are used with the dynamic subgrid-scale turbulence model described earlier. Preliminary simulations run with the coarser grid without the turbulence model showed the appearance of strong wiggles and gave results in poor agreement with the experiments.

Examples of instantaneous computed fields are given in Fig. 6. There it can be seen that structure is generated on scales as

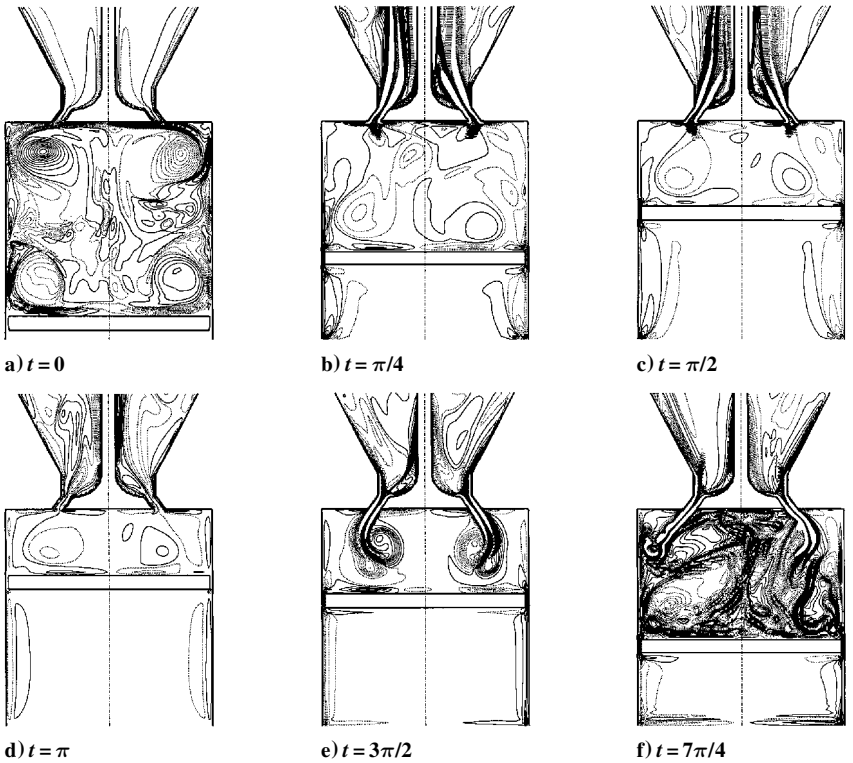

Fig. 5 Contour plots of azimuthal vorticity for a three-dimensional case with azimuthal perturbation at $Re = 315,97 \times 85 \times 193$ ($\theta \times r \times z$) grid, no turbulence model; the vorticity scale is the same as in Fig. 3.

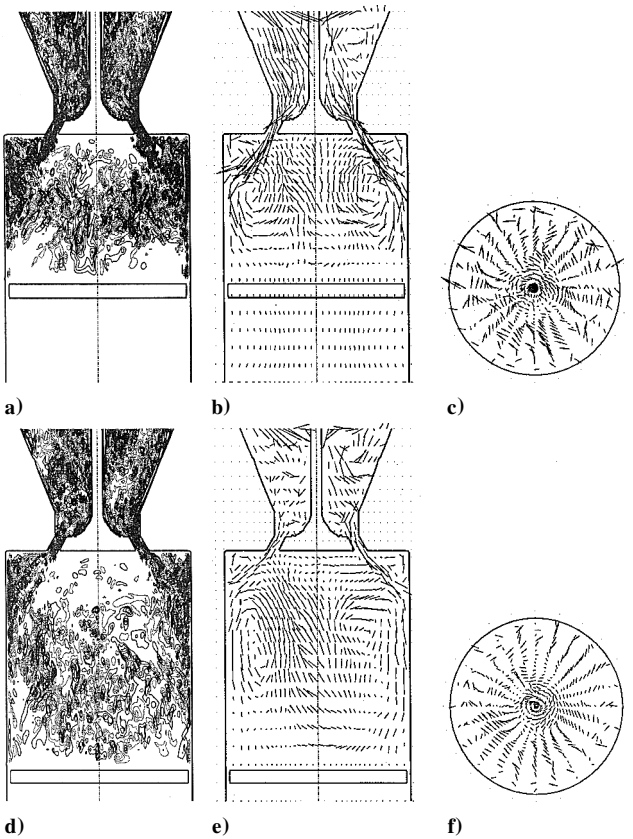

Fig. 6 Contour plots of azimuthal vorticity and velocity vectors projected onto two-dimensional cutting planes for a three-dimensional case with azimuthal perturbation at $Re = 2000$, $65 \times 65 \times 151$ ($\theta \times r \times z$) grid, dynamic Smagorinsky subgrid-scale turbulence model; vorticity scale is the same as in Fig. 3: a) $t = \pi/2$, aximuthal vorticity; b) $t = \pi/2$, projected velocity vectors, meridional plane; c) $t = \pi/2$, projected velocity vectors, 15 mm below the head; d) $t = \pi$, aximuthal vorticity; e) $t = \pi$, projected velocity vectors, meridional plane; and f) $t = \pi$, projected velocity vectors, 15 mm below the head.

small as can be supported on the computational grid. Still, the underlying large-scale flow pattern seen in the axisymmetric simulations (Fig. 3) remains discernible. The motion in meridional planes (planes containing the geometric axis of symmetry) is coupled with intense azimuthal velocity fluctuations whose magnitude is comparable with the axial velocity fluctuations. As was the case for the low-Reynolds-number, three-dimensional simulation with initial perturbation (Fig. 5), this flow is time periodic only in a statistical sense. The calculation of statistically converged mean quantities in general requires phase averaging. However, the axisymmetric nature of the geometry allows azimuthal averaging to be used as well to reduce the number of cycles that must be computed.

Quantitative comparison between computation on the finer grid and experimental measurement is reported in Figs. 7 and 8. Figure 7 shows radial profiles of mean and rms axial velocity at 36 deg after TDC. Three sets of profiles, 10, 20, and 30 mm below the head, are shown. The numerical results are phase averaged over three piston cycles, and are azimuthally averaged as well, to obtain stable statistics. Although the rms profiles might benefit from some additional averaging, both the mean and the rms profiles already show good agreement with measurements. Figure 8 shows the same information at a later crank position of 144 deg after TDC; again the agreement is quite satisfactory. In fact, the level of agreement between the present computations and the experiment is better than any results that have been published using a RANS model.[20]

Also shown in Figs. 7 and 8 are results from two other LES modeling studies where an unstructured, boundary-fitted, deforming-grid method was used.[7,19] There the discretization was second order in space and in time, the advection scheme was dissipative (upwind-biased), and the fully compressible form of the governing equations was solved.[30] One set corresponds to a coarse mesh (151,620 nodes) and a constant-coefficient Smagorinsky model ($C = 0.1^2$); the other set used a somewhat finer mesh (258,264 nodes) and a dynamic Smagorinsky model with Lagrangian averaging.[31]

Both the present results and the fine-mesh, dynamic-model, unstructured results show better agreement with measurements compared to the coarse-mesh, fixed-coefficient, unstructured results, for example, 36 deg, 20 mm below head. The present method yields consistently higher rms values than the fine-mesh, dynamic-model, unstructured results at measurement stations close to the head, for

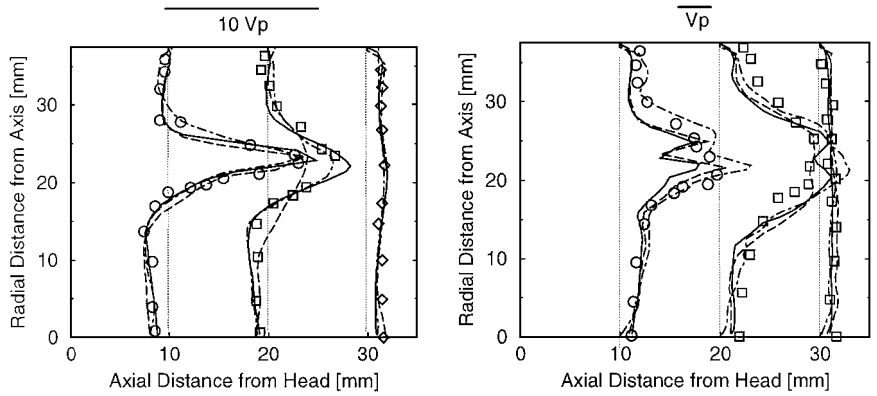

a) Mean velocity b) RMS velocity

Fig. 7 Computed and measured radial profiles of mean and rms axial velocity at 36 deg ($Re = 2000$). Lines are computations: – – –, unstructured boundary-fitted deforming grid, 150 K nodes, fixed-coefficient Smagorinsky[6,19]; ——, unstructured boundary-fitted deforming grid, 260,000 nodes, Lagrangian dynamic Smagorinsky[6,19]; and — · —, fixed orthogonal grid with boundary body forces, 640,000 nodes, dynamic Smagorinsky (present work); symbols are experimental measurements.[18]

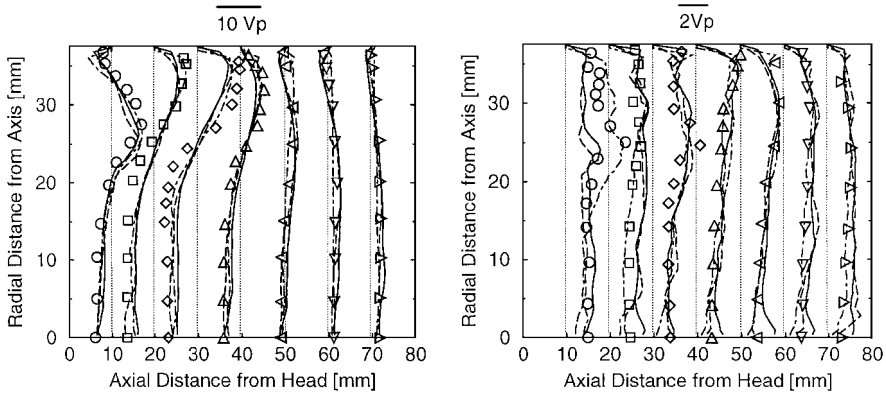

a) Mean velocity b) RMS velocity

Fig. 8 Computed and measured radial profiles of mean and rms axial velocity at 144 deg ($Re = 2000$); lines and symbols are the same as in Fig. 7.

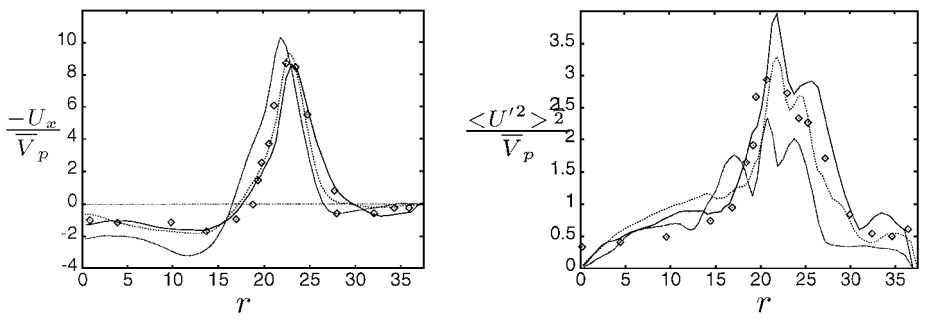

a) Mean velocity b) RMS velocity

Fig. 9 Computed and measured radial profiles of mean and rms axial velocity at 36 deg, 10 mm below the head ($Re = 2000$); lines are computations: ——, dynamic Smagorinsky model and fine grid ($97 \times 85 \times 193$); – – –, dynamic Smagorinsky model and coarse grid ($65 \times 65 \times 151$); and ——, fixed-coefficient Smagorinsky model and coarse grid ($65 \times 65 \times 151$); symbols are experimental measurements.[18]

example, 144 deg, 10 mm below head. Because comparable dynamic subgrid-scale models have been used, the higher rms values for the present method probably result from a combination of the finer mesh and the nondissipative numerical scheme.

The computational-efficiency advantage of the present method is substantial. The present incompressible, boundary-body-force, three-dimensional, turbulent cases were run on a personal computer-like workstation with 128 MB of RAM in about one week using a grid of approximately 6×10^5 nodes (about 24 h per engine cycle). By contrast, the compressible, unstructured, boundary-fitted, deforming-grid, coarse-mesh cases ($\approx 1.5 \times 10^5$ nodes) were run either on a single processor of a Cray T-90 or on eight processors of a SGI Origin 2000, occupied 600 MB of RAM, and required 30–40 CPU h per engine cycle.

Before concluding this section, a few further three-dimensional turbulent results obtained using the boundary-body-force methodology are discussed. These include variations in grid density and subgrid-scale turbulence model. Examples of coarser-grid results for a fixed coefficient and for a dynamic Smagorinsky model are reported. In particular, in Fig. 9, results are shown also for a simulation on a $65 \times 65 \times 151$ grid with two different subgrid-scale turbulence models. The two simulations with the dynamic Smagorinsky model and different grids must be intended as a grid refinement check. We can see that the results agree within the the statistical uncertainty, thus proving the grid independency. In addition, the dynamic model behaves consistently with the expectations, in the sense that the model becomes more active (adds more viscosity) as the grid is coarsened. Differences between the constant-coefficient

Smagorinsky model ($C = 0.2^2$) and the dynamic Smagorinsky model are more significant. The fixed-coefficient model yields a more peaked annular jet and damped velocity fluctuations (lower rms). This behavior is consistent with the more dissipative nature of the constant-coefficient model. This result was obtained for a single value of the model constant C; improved results might be obtained with tuning. However, it is unlikely that a single value of the model constant would prove sufficient in a flow that is so highly nonhomogeneous both in space and in time.

Conclusions

A computationally efficient numerical and modeling approach has been demonstrated for LES of turbulent flows in complex geometric configurations with moving boundaries. The technique is based on the use of boundary body forces to represent solid walls. The body forces are prescribed on a fixed, structured, orthogonal mesh in a manner that allows the representation of arbitrarily complex moving boundary surfaces. The forcing does not reduce the stability limit of the underlying time-integration scheme. Thus, this approach retains the advantages of solving the Navier–Stokes equations in constant-metric coordinates. Compared to unstructured, boundary-fitted, deforming-grid LES, the present method simplifies grid generation, facilitates the implementation of higher-order nondissipative discretization schemes, and minimizes complications that arise from spatial and temporal variations in filter width for LES.

The method has been validated via the LES of a turbulent flow in an axisymmetric motored piston–cylinder assembly. Computed results show very good quantitative agreement with experimental measurements, and computational requirements are substantially reduced compared to simulations that used a (compressible) unstructured, boundary-fitted, deforming-mesh approach.

The dynamic subgrid-scale turbulence model is particularly well suited to the present numerical methodology. This model automatically accounts for the presence of solid walls without requiring damping functions. There is no need to compute a wall-normal distance that would be, in the present approach, much more difficult than in the case of a body-fitted mesh.

Acknowledgments

This work was carried out during the 1998 Summer Program of the Stanford University/NASA Ames Research Center, Center for Turbulence Research (CTR); the authors gratefully acknowledge CTR's financial support. The first author acknowledges the European Research Office, U.S. Army, for partial support under Contract N68171-98-M-5645. We are indebted to M. Fatica for numerous suggestions and for providing help in the numerical simulations and postprocessing. We also thank W. H. Cabot for advice in implementing the dynamic large eddy simulation model in the code.

References

[1]Jiménez, J., Wray, A. A., Saffman, P. G., and Rogallo, R. S., "The Structure of Intense Vorticity in Isotropic Turbulence," *Journal of Fluid Mechanics*, Vol. 255, Oct. 1993, pp. 65–90.

[2]Kim, J., Moin, P., and Moser, R. D., "Turbulence Statistics in Fully Developed Channel Flow at Low Reynolds Number," *Journal of Fluid Mechanics*, Vol. 177, April 1987, pp. 133–166.

[3]Moser, R. D., and Rogers, M. M., "The Three-Dimensional Evolution of a Plane Mixing Layer: Pairing and Transition to Turbulence," *Journal of Fluid Mechanics*, Vol. 247, Feb. 1992, pp. 275–320.

[4]Choi, H., Moin, P., and Kim, J., "Direct Simulation of Turbulent Flow Over Riblets," *Journal of Fluid Mechanics*, Vol. 255, Oct. 1993, pp. 503–539.

[5]Ferziger, J. H., and Peric, M., *Computational Methods for Fluid Dynamics*, Springer–Verlag, New York, 1996, p. 356.

[6]Galperin, B., and Orzsag, S. A. (eds.), *Large-Eddy Simulation of Complex Engineering and Geophysical Flows*, Cambridge Univ. Press, New York, 1993, p. 600.

[7]Haworth, D. C., "Large-Eddy Simulation of In-Cylinder Flows," *Multidimensional Simulation of Engine Internal Flows*, Institut Francais du Petrol, Rueil-Malmaison, France, 1998.

[8]Peskin, C. S., "Flow Patterns Around Heart Valves: a Numerical Method," *Journal of Computational Physics*, Vol. 10, Oct. 1972, pp. 252–271.

[9]Goldstein, D., Handler, R., and Sirovich, L., "Modeling a No-Slip Flow Boundary with an External Force Field," *Journal of Computational Physics*, Vol. 105, April 1993, pp. 354–366.

[10]Saiki, E. M., and Biringen, S., "Numerical Simulation of a Cylinder in Uniform Flow: Application of a Virtual Boundary Method," *Journal of Computational Physics*, Vol. 123, Feb. 1996, pp. 450–465.

[11]Roache, P. J., *Computational Fluid Dynamics*, Hermosa, Albuquerque, NM, 1976, p. 446.

[12]Mohd-Yusof, J., "Interaction of Massive Particles with Turbulence," Ph.D. Dissertation, Dept. of Mechanical and Aerospace Engineering, Cornell Univ., Ithaca, NY, 1996.

[13]Mohd-Yusof, J., "Combined Immersed-Boundary/B-Spline Methods for Simulations of Flows in Complex Geometries," *CTR Annual Research Briefs*, NASA Ames Research Center/Stanford Univ. Center for Turbulence Research, Stanford, CA, 1997, pp. 317–327.

[14]Mohd-Yusof, J., and Lumley, J. L., "Simulation of Flow Around Cylinders Using Boundary Forcing," *Bulletin of the American Physical Society*, Vol. 39, No. 9, 1994, p. 1871.

[15]Mohd-Yusof, J., and Lumley, J. L., "Improved Immersed Boundary Techniques for Complex Flows," *Bulletin of the American Physical Society*, Vol. 41, No. 9, 1996, p. 1700.

[16]Fadlun, E. A., Verzicco, R., Orlandi, P., and Mohd-Yusof, J., "Combined Immersed Boundaries/Finite-Difference Methods for Three-Dimensional Complex Flow Simulations," *Journal of Computational Physics* (submitted for publication).

[17]Fadlun, E. A., Verzicco, R., and Orlandi, P., "Flussi in Geometrie Complesse con Forze di Massa su Griglie Cartesiane: Simulajioni Numeriche e Validazione Sperimentale," M.S. Thesis, Dept. Meccanica and Aeronautica, Univ. of Rome "La Sapienza Rome," Rome, 1998 (in Italian).

[18]Morse, A. P., Whitelaw, J. H., and Yianneskis, M., "Turbulent Flow Measurement by Laser Doppler Anemometry in a Motored Reciprocating Engine," Dept. of Mechanical Engineering, Rept. FS/78/24, Imperial College of Science, Technology, and Medicine, London, 1978.

[19]Haworth, D. C., and Jansen, K., "Large-Eddy Simulation on Unstructured Deforming Meshes: Towards Reciprocating IC Engines," *Computers and Fluids* (submitted for publication).

[20]El Tahry, S. H., and Haworth, D. C., "Directions in Turbulence Modeling for In-Cylinder Flows in Reciprocating IC Engines," *Journal of Propulsion and Power*, Vol. 8, No. 5, 1992, pp. 1040–1048.

[21]Germano, M., Piomelli, U., Moin, P., and Cabot, W. H., "A Dynamic Subgrid-Scale Eddy Viscosity Model," *Physics of Fluids A*, Vol. 3, July 1991, pp. 1760–1765.

[22]Lilly, D. K., "A Proposed Modification of the Germano Subgrid-Scale Closure Method," *Physics of Fluids A*, Vol. 4, March 1992, pp. 633–635.

[23]Moin, P., and Kim, J., "Numerical Investigation of Turbulent Channel Flow," *Journal of Fluid Mechanics*, Vol. 118, May 1982, pp. 341–377.

[24]Verzicco, R., and Orlandi, P., "A Finite-Difference Scheme for Three-Dimensional Incompressible Flow in Cylindrical Coordinates," *Journal of Computational Physics*, Vol. 123, Feb. 1996, pp. 402–413.

[25]Orlandi, P., and Fatica, M., "Direct Simulations of a Turbulent Pipe Rotating Along the Axis," *Journal Fluid Mechanics*, Vol. 343, July 1997, pp. 43–72.

[26]Mittal, R., and Moin, P., "Suitability of Upwind-Biased Finite Difference Schemes for Large-Eddy Simulation of Turbulent Flows," *AIAA Journal*, Vol. 35, No. 8, 1997, pp. 1415–1417.

[27]Swartzrauber, P. N., "A Direct Method for the Discrete Solution of Separable Elliptic Equations," *SIAM Journal of Numerical Analysis*, Vol. 11, Dec. 1974, pp. 1136–1150.

[28]Eaton, A. R., and Reynolds, W. C., "High-Speed Photography of Smoke-Marked Flow in a Motored Axisymmetric Engine," American Society of Mechanical Engineers, Paper 87-FE-10, Feb. 1987.

[29]Eaton, A. R., and Reynolds, W. C., "Flow Structure and Mixing in a Motored Axisymmetric Engine," Society of Automotive Engineers, Paper 890321, Feb.–March 1989.

[30]O'Rourke, P. J., and Sahota, M. S., "A Variable Explicit/Implicit Numerical Method for Calculating Advection on Unstructured Grids," *Journal of Computational Physics*, Vol. 143, No. 2, 1998, pp. 312–345.

[31]Meneveau, C., Lund, T. S., and Cabot, W. H., "A Lagrangian Dynamic Subgrid-Scale Model of Turbulence," *Journal of Fluid Mechanics*, Vol. 319, July 1996, pp. 353–385.

P. Givi
Associate Editor